

Emergence of intrinsically isolated flat bands and their topology in fully relaxed twisted multi-layer graphene

Xianqing Lin,^{1,*} Haotian Zhu,¹ and Jun Ni²

¹College of Science, Zhejiang University of Technology, Hangzhou 310023, People's Republic of China

²State Key Laboratory of Low-Dimensional Quantum Physics and Frontier Science Center for Quantum Information, Department of Physics, Tsinghua University, Beijing 100084, People's Republic of China

(Dated: September 15, 2024)

We study the electronic structure and band topology of fully relaxed twisted multi-layer graphene (TMLG). Isolated flat bands emerge in TMLG with the number of layers [$M + N$ with M the layer number of the bottom few-layer graphene (FLG)] up to 10 and with various stacking orders, and most of them are on the hole side. The touched bands of FLGs around the Fermi level are split by the moiré coupling through the electron-hole asymmetry in low-energy bands of FLGs and by the vertical hopping between next-nearest layers. The full structural relaxation leads to global gaps that completely isolate a flat band. For TMLG with given M and N , the highest magnitude of Chern numbers ($|C|$) of the separable flat bands reaches $M + N - 1$ and can be hosted by certain isolated bands. The $|C| = 9$ occurs in the isolated flat valence band of several configurations with 10 layers. Such high $|C|$ originates from the lifting of the band-state degeneracy in the weak regime of moiré coupling or from the topological phase transitions induced by the strong moiré coupling. Moreover, large orbital magnetic moments arise in isolated flat bands with high $|C|$ and depend on the structural configurations of TMLG.

I. INTRODUCTION

The emergence of low-energy flat bands¹⁻⁴ and the observation of associated superconductivity and correlated-insulator phases⁵⁻¹² in magic-angle twisted bilayer graphene (TBG) have inspired great interest in exploring the peculiar electronic structure of graphene moiré systems^{13,14}. Finite Berry phases around the Dirac cones of monolayer graphene are maintained in TBG¹⁵⁻¹⁸, while the breaking of C_2T symmetry is required to obtain separable flat bands with nontrivial Chern numbers (C)¹⁹⁻²¹, which can be achieved by carefully aligning TBG with hexagonal boron nitride to commensurate twist angles between them²²⁻²⁶. In such heterostructures, quantized anomalous Hall conductivity (QAHC) $\sigma_{xy} = Ce^2/h$ is observed at an odd filling of a flat band together with spontaneous orbital ferromagnetism^{27,28}. QAHC with $|C| = 2$ has been realized in chirally stacked trilayer graphene aligned with BN²⁹. In contrast to TBG, intrinsic flat Chern bands in a valley arise in BA-AB stacked twisted double bilayer graphene (TDBG) and their $|C|$ can reach 3³⁰⁻³⁵. This suggests that higher-order flat Chern bands may occur in thicker twisted multi-layer graphene (TMLG) composed of two few-layer graphene (FLGs) with relative rotation. Moreover, complete isolation of a flat Chern band by global gaps from other bands is also essential to obtain QAHC that is contributed purely by edge states²⁵. Therefore, it is important to explore TMLG systematically to identify isolated flat bands with high-order topology in graphene moiré systems.

The electronic structure of TMLG depends on the stacking orders of the FLGs and the twist angle (θ)^{32,36-41}. The flat bands around the Fermi level (E_F) of TMLG were found to be entangled with each other or with other dispersive bands by band crossings^{32,38-41}.

Most studies introduced external electric field to separate the flat bands so that their band topology becomes well defined, while the produced C is limited to small values^{39,41}. For TMLG composed of chirally stacked FLGs, the flat valence and conduction bands in a valley can be separated from other bands and their total C were demonstrated to increase with the layer numbers of TMLG³². This suggests that high C may occur in one flat band if it can become isolated. We note that only rigid moiré superlattices of TMLG were considered in these previous studies^{32,38-41}, while full relaxation has been shown to be able to enhance the band separation in TBG and TDBG^{35,42-46}. In addition, the interlayer coupling was limited to that between adjacent layers^{32,38-41}. The coupling between next-nearest layers may also play an important role to isolate the flat bands.

Here, we have identified various stacking orders of fully relaxed TMLG with isolated flat bands. Certain isolated flat valence bands in configurations with $M + N$ layers can host $|C|$ as large as $M + N - 1$ and also large orbital magnetic moments for $M + N$ up to 10. The mechanism behind the emergence of isolated flat bands and their significant band topology have been revealed.

II. STRUCTURAL CONFIGURATIONS OF TMLG

We study TMLG with the top FLG (tFLG) rotated by θ counterclockwise and the bottom FLG (bFLG) fixed, as seen in Fig. 1(a). The layer numbers of bFLG and tFLG are denoted by M and N , respectively. We consider the strictly periodic moiré superlattices of TMLG with $M + N$ up to 10 and θ from 1.890° to 1.018° . Starting from the twist interface, the layers in bFLG and tFLG are indexed by $n = 1 \sim M$ and $\tilde{n} = \tilde{1} \sim \tilde{N}$, respectively.

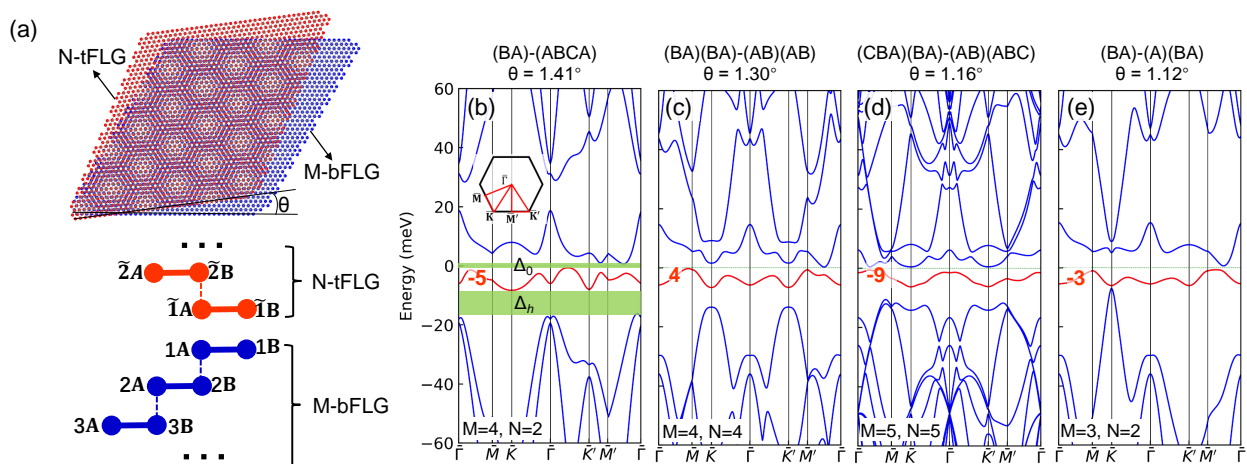


FIG. 1. (Color online) The geometry and electronic band structures of TMLG. (a) The schematic view of the TMLG with the top FLG (tFLG) rotated by θ counterclockwise with respect to the bottom FLG (bFLG). The shown side view is around the AA stacking between layers 1 and $\tilde{1}$. The layer numbers of bFLG and tFLG are denoted by M and N , respectively. The sublattices in each layer are labeled by $n\alpha$ with n the layer index and $\alpha=A, B$. (b-e) The band structures with isolated flat valence bands (red lines) for typical configurations of the four stacking types of TMLG. As bands in the two valleys are related by the time reversal symmetry, only bands in the $\xi = +$ valley are displayed. The isolated valence band is separated from other bands by global gaps Δ_0 and Δ_h labeled in (b). The Chern numbers of the isolated bands in the $\xi = +$ valley are labeled. The Fermi levels are represented by dashed lines.

Besides the tunable θ , there exist 2^{M+N-3} inequivalent stacking orders for TMLG with $M + N$ layers, which are represented by the stackings of tFLG and bFLG. For example, a configuration composed of tFLG with the BA stacking and bFLG with the ABCA stacking is denoted by BA-ABCA. The geometry of moiré superlattices in TMLG is detailed in the Supplemental Material (SM).

Within a FLG, a pair of sites from two adjacent layers with one site directly above the other are referred to as dimer sites, and there is a relatively strong interlayer hopping (γ_1) between them. In a chirally stacked FLG, the sites in inner layers are all dimer sites, and the non-dimer sites which constitute the low-energy band states are on the surface layers^{47,48}. For a general stacking of FLG, the layers can be decomposed into a sequence of chiral subsets^{39,40,49,50}, which are represented as chiral stacking orders in parentheses, such as (AB)(ABC). Such chiral decomposition of tFLG and bFLG in TMLG determines some characters of the electronic structure.

In TMLG, the local stacking between layer $\tilde{1}$ of tFLG and layer 1 of bFLG varies continuously across the moiré superlattice. Then the optimal local spacing between these layers determined by the local stacking also varies with the in-plane position in the superlattice, leading to the corrugation of the layers. More importantly, the spatially varying potential at the twist interface can drive the in-plane structural relaxation. Full relaxation has been performed for each configuration of TMLG employing the continuum elastic theory, as detailed in the SM.

III. ELECTRONIC STRUCTURE OF TMLG

For each relaxed configuration of TMLG, we have built a tight-binding Hamiltonian (\hat{H}) taking into account the effects of out-of-plane corrugation and in-plane structural deformation. The Hamiltonian parameters and computational approaches of the electronic structure are given in the SM. It is noted that the vertical next-nearest-layer hopping (γ_2) within the top and bottom FLGs is included in \hat{H} . To diagonalize \hat{H} , the plane-wave-like basis functions are adopted and denoted by $|n\alpha, \mathbf{k}\rangle$, where n is the layer index, $\alpha = A, B$, and \mathbf{k} represents the momentum of the state in the reciprocal space of the pristine FLGs.

By calculating the two-dimensional (2D) energy bands in the entire Brillouin zone (BZ) for relaxed TMLG with different θ and stackings, we find that completely isolated flat bands emerge around E_F for various configurations of TMLG, even for those with 10 layers. We consider flat bands with widths smaller than 10 meV. For an isolated band, global gaps are opened above and below this band. The bands around E_F show rather strong electron-hole asymmetry and most isolated flat bands are on the hole side. The stacking orders that host isolated flat valence bands in a relatively large range of θ are listed in Table I and those with flat valence bands that are only isolated at some θ can be seen in Table SI of the SM. Figure 1(b-e) show the band structures of four typical configurations with different types of stacking orders and their DOS can be seen in Fig. S3. Since only very few configurations have isolated flat conduction bands (see Table SII), we focus on isolated flat valence bands in the following.

Through examination of variations of the electronic

TABLE I. The stacking orders that host isolated flat valence bands in a relatively large range of θ : the total layer numbers ($M + N$), the layer numbers of bFLG (M) and tFLG (N), the stacking type, the twist-angle range from θ_1 to θ_2 with isolated flat valence bands, the values of W_v , Δ_h , and Δ_0 in units of meV at θ_1 and θ_2 , and the Chern numbers (C_v) of the flat valence bands for twist angle from θ_1 to θ_2 .

$M + N$	M	N	stacking	type	θ_1	$W_v^{(1)}$	$\Delta_h^{(1)}$	$\Delta_0^{(1)}$	θ_2	$W_v^{(2)}$	$\Delta_h^{(2)}$	$\Delta_0^{(2)}$	C_v
4	2	2	(BA)-(AB)	I	1.35°	9.9	23.9	0.8	1.02°	4.1	5.6	2.7	-3,0,-2
5	3	2	(BA)-(A)(BA)	IV	1.30°	5.4	0.8	1.3	1.02°	4.7	0.7	2.0	0,-3,-2
6	3	3	(AB)(A)-(A)(BA)	IV	1.30°	5.4	0.6	1.6	1.02°	4.5	0.8	2.2	0,-3,-2
6	4	2	(BA)-(AB)(AB)	II	1.30°	6.7	5.7	1.1	1.02°	6.1	4.8	2.2	2,-1,0
6	4	2	(CA)-(AB)(AB)	II	1.35°	9.6	4.0	0.1	1.05°	8.3	4.2	1.2	2,5
6	4	2	(BA)-(ABCA)	I	1.47°	8.9	9.5	1.4	1.35°	8.3	4.9	0.5	-5
7	5	2	(BA)-(AB)(ABC)	III	1.30°	4.9	1.4	1.4	1.02°	4.0	0.3	0.1	-3,-6,-5
7	5	2	(CA)-(AB)(ABC)	III	1.25°	6.3	1.4	0.4	1.08°	4.8	0.5	0.5	0
8	4	4	(BA)(BA)-(AB)(AB)	II	1.30°	7.1	5.7	0.5	1.02°	6.2	4.9	2.2	4,1,2
8	5	3	(AB)(A)-(AB)(ABC)	IV	1.30°	4.8	0.8	1.7	1.12°	5.0	0.7	0.5	-3,-6
8	6	2	(BA)-(A)(BA)(BAC)	IV	1.30°	4.7	0.8	1.6	1.02°	4.1	0.5	1.9	3,0,1
9	6	3	(AB)(A)-(A)(BA)(BAC)	IV	1.30°	4.7	0.7	1.8	1.02°	4.7	0.6	1.5	3,0,1
9	7	2	(BA)-(A)(BA)(CABC)	IV	1.25°	6.1	1.1	0.7	1.02°	4.8	0.6	0.1	-4,-7,-6
10	5	5	(CBA)(BA)-(AB)(ABC)	III	1.30°	5.2	1.4	0.9	1.12°	5.5	0.6	0.2	-6,-9
10	7	3	(AB)(A)-(A)(BA)(CABC)	IV	1.30°	5.4	0.8	0.9	1.02°	4.8	0.5	0.1	-4,-7,-6

properties with different configurations of TMLG, we categorize the stacking orders into four types, i.e. cases with chirally stacked FLGs (type I), those with Bernal-stacked FLGs that have even numbers of layers (type II), other cases without a single layer in the stacking decomposition of FLGs (type III) and with a single layer in decompositions (type IV), as listed in Tables I and SI. The isolated flat valence band is separated from other bands by global gaps at the charge neutrality point (Δ_0) and just below it (Δ_h). Δ_0 is smaller than 4 meV for all cases, while Δ_h can have a rather large value, especially for type-I cases, as shown in Fig. 2(a). Most type-IV configurations have extremely narrow Δ_h as some characters of the low-energy linear dispersions contributed by the decomposed single layer in the pristine FLGs are maintained. The Δ_h of most type-II cases are quite large, while those of many type-III cases are rather small. The widths (W_v) of isolated valence bands begin to become smaller than 10 meV at $\theta \approx 1.5^\circ$, as shown in Fig. 2(b). For type-I cases, W_v can be narrower than 5 meV only when θ is around or below 1.1° , while the W_v of type-III and type-IV cases can reach such narrow W_v at about 1.3° . The electronic behavior of different stacking types also depends on the thickness of TMLG. Only when $N + M \leq 7$, isolated flat bands can emerge for type-I stacking, as seen in Table II. For $N + M \geq 9$, only type-III and type-IV cases can have isolated flat bands. No isolated flat bands exist for systems with $N = 1$. In addition, similar to pristine FLGs^{47,48}, the 2D energy dispersions of the isolated flat bands exhibit trigonal warping, as seen in Fig. S2.

To reveal the mechanism behind the emergence of isolated flat bands in TMLG, we have compared the band structures and state composition of some configurations with different parts of the Hamiltonian, as shown in Fig. 3 for the type-I (BA)-(ABCA) stacking and the type-II (CA)-(AB)(AB) stacking at $\theta = 1.35^\circ$. Starting from the

rigid superlattice without moiré coupling between FLGs and without the γ_2 hopping within FLGs, the moiré coupling, the γ_2 hopping, the corrugation effect, and the in-plane relaxation effect are included in the Hamiltonian successively.

Without moiré coupling, the low-energy bands of bFLG (tFLG) touch at the corner \bar{K} (\bar{K}') [see Fig. S1(b)] of the supercell BZ, and the bands of bFLG cross with those of tFLG, as seen in Figs. 4(a), 4(f) and S4. The band crossings can be eliminated by the moiré hopping between layers 1 and $\bar{1}$ in a way similar to TBG, as these degenerate states at crossings have contributions from these interface layers. In contrast to TBG always with touched valence and conduction bands at the BZ corners, state splitting occurs around E_F upon inclusion of the moiré coupling for TMLG. In the pristine bFLG, the states composed of non-dimer sites have zero energy at \bar{K} . These states are just the non-dimer basis functions with the momentum of K_+ , which is at the corner of the bFLG BZ [see Fig. S1(a)]. When bFLG is coupled to tFLG, the energy of the non-dimer state ($|1B, K_+\rangle$) in the first layer of bFLG rises above zero and the other non-dimer states still have zero energy. We will show that the positive energy of $|1B, K_+\rangle$ is due to the electron-hole asymmetry in low-energy bands of tFLG.

For the chiral tFLG whose zero-energy states are at \bar{K}' , three degenerate conduction states ($|\psi_{c,n}\rangle$ with $n = 1 - 3$) and three degenerate valence states ($|\psi_{v,n}\rangle$) have low energies ($\varepsilon_{c,n}$ and $\varepsilon_{v,n}$) at \bar{K} , as seen in Fig. S4. By second-order perturbation approximation, the energy (ε_{1B}) of $|1B, K_+\rangle$ can be expressed as

$$\varepsilon_{1B} = \sum_{n=1}^3 \frac{|\langle 1B, K_+ | \hat{H} | \psi_{c,n} \rangle|^2}{-\varepsilon_{c,n}} + \sum_{n=1}^3 \frac{|\langle 1B, K_+ | \hat{H} | \psi_{v,n} \rangle|^2}{-\varepsilon_{v,n}} \quad (1)$$

Considering only the interlayer hopping γ_1 between

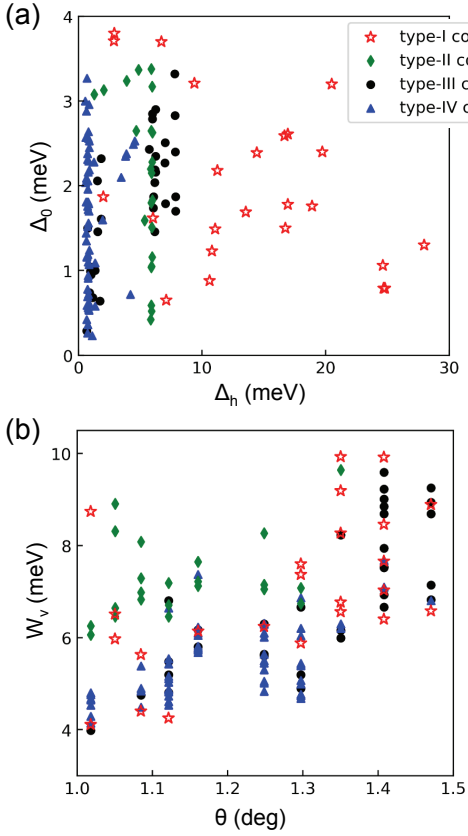


FIG. 2. (Color online) The properties of isolated flat valence bands in configurations with different stacking types. (a) Δ_0 and Δ_h for all configurations with isolated flat valence bands. Each configuration of TMLG is characterized by the stacking and θ . (b) Width (W_v) of the isolated valence band versus θ of these configurations.

dimer sites, the bands of tFLG are electron-hole symmetric. Then all $|\langle 1B, K_+ | \hat{H} | \psi_{c,n} \rangle|$ and $|\langle 1B, K_+ | \hat{H} | \psi_{v,n} \rangle|$ have the same value. One of $|\psi_{c,n}\rangle$ is expanded in the basis functions with momentum at K_+ including $|\tilde{1}\alpha, K_+\rangle$ ($\alpha = A, B$) in layer $\tilde{1}$ of tFLG. For the rigid superlattice, the moiré coupling between layers 1 and $\tilde{1}$ produces the same value (u) of the Hamiltonian elements between $|1B, K_+\rangle$ and $|\tilde{1}\alpha, K_+\rangle$. For the BA stacked tFLG, $|\langle 1B, K_+ | \hat{H} | \psi_{c,n} \rangle|$ becomes $u/\sqrt{2}$ as layer $\tilde{1}$ contributes half of the squared norm of $|\psi_{c,n}\rangle$. For other tFLG, $|\langle 1B, K_+ | \hat{H} | \psi_{c,n} \rangle|$ decreases slowly with its number of layers. With the electron-hole symmetry, $\varepsilon_{v,n} = -\varepsilon_{c,n}$, then ε_{1B} is still zero.

The interlayer hopping γ_4 between a non-dimer site and a dimer site introduces electron-hole asymmetry in the bands of FLGs. The supercell momentums of the basis functions expanding $|\psi_{v,n}\rangle$ and $|\psi_{c,n}\rangle$ all have the same length $k_\theta \approx 4\pi\theta/3a$. With only γ_1 and γ_4 as well as the intralayer nearest-neighbor hopping ($-t_0$) for chiral tFLG with N layers, $\varepsilon_{v,n}$ and $\varepsilon_{c,n}$ can be expressed

analytically as^{47,48}

$$\begin{aligned} \varepsilon_{v,n} &= -(\sqrt{3}t_0ak_\theta/2)^N/\gamma_1^{N-1} + 3t_0\gamma_4a^2k_\theta^2/(2\gamma_1), \\ \varepsilon_{c,n} &= (\sqrt{3}t_0ak_\theta/2)^N/\gamma_1^{N-1} + 3t_0\gamma_4a^2k_\theta^2/(2\gamma_1), \end{aligned} \quad (2)$$

which lead to $-\varepsilon_{v,n} < \varepsilon_{c,n}$. Numerical calculations show that $\varepsilon_{v,n}$ is also closer to zero than $\varepsilon_{c,n}$ for non-chiral FLGs. In addition, the norms of all the Hamiltonian elements in Eq. (1) are still approximately equal when including γ_4 . Therefore, ε_{1B} has a positive value. For the BA stacked tFLG, ε_{1B} is given analytically by

$$\varepsilon_{1B} = \frac{u^2}{\theta^2} \frac{9\gamma_1}{8\pi^2 t_0^2} \left(\frac{1}{1 - 2\gamma_4/t_0} - \frac{1}{1 + 2\gamma_4/t_0} \right). \quad (3)$$

As γ_4 is much smaller than t_0 , we have $\varepsilon_{1B} \approx 9\gamma_1\gamma_4u^2/(2\pi^2t_0^3\theta^2)$.

At \bar{K}' , similar analysis shows that the positive energy of the non-dimer state $|\tilde{1}B, K'_+\rangle$ in layer $\tilde{1}$ of tFLG can also be attributed to the electron-hole asymmetry in the bands of bFLG.

When only moiré coupling is included in the Hamiltonian of the (CA)-(AB)(AB) configuration with non-chiral bFLG, three states contributed by the non-dimer sites in the bottom three layers of bFLG still have zero energy at \bar{K}' , as seen in Fig. 3(g). The turning on of the γ_2 hopping between the 2A and 4A sites can split these degenerate states, as shown in Fig. 3(h). Then only the $|\tilde{3}B, K'_+\rangle$ state is located at almost zero energy.

For the rigid superlattice with all interlayer hopping, the flat bands around E_F remain overlapped with other dispersive bands. The corrugation effect reduces such band overlapping by making the flat valence band narrower, as shown in Figs. 3(d) and 3(i). The in-plane relaxation has a more significant impact on the band dispersions. The flat valence band can become completely gapped from other bands with full relaxation, while Δ_0 may be decreased by the in-plane relaxation, especially for configurations with a non-chiral FLG, as shown in Figs. 3(e) and 3(j).

To further demonstrate the importance of full relaxation for the emergence of isolated flat bands, the variations of W_v , Δ_h and Δ_0 with θ considering both out-of-plane and in-plane relaxation are compared with those considering only corrugation in Fig. 4. For (BA)-(ABCA) with only corrugation effect, W_v is overestimated at θ around 1.1° , Δ_h is underestimated at all θ , and Δ_0 is also underestimated at small θ . For (CA)-(AB)(AB), only with full relaxation can Δ_h and Δ_0 become positive at small θ . The trends of these electronic properties with θ are also rather different for the two stackings. In particular, the maximum value of Δ_h is located at about 1.5° for (BA)-(ABCA), while it is at about 1.2° for (CA)-(AB)(AB). In addition, the first local minimum of W_v is also at a larger θ for (BA)-(ABCA).

We have focused on TMLG without potential differences between layers. It is noted that equal potential differences (Δ) between adjacent layers produced by applied

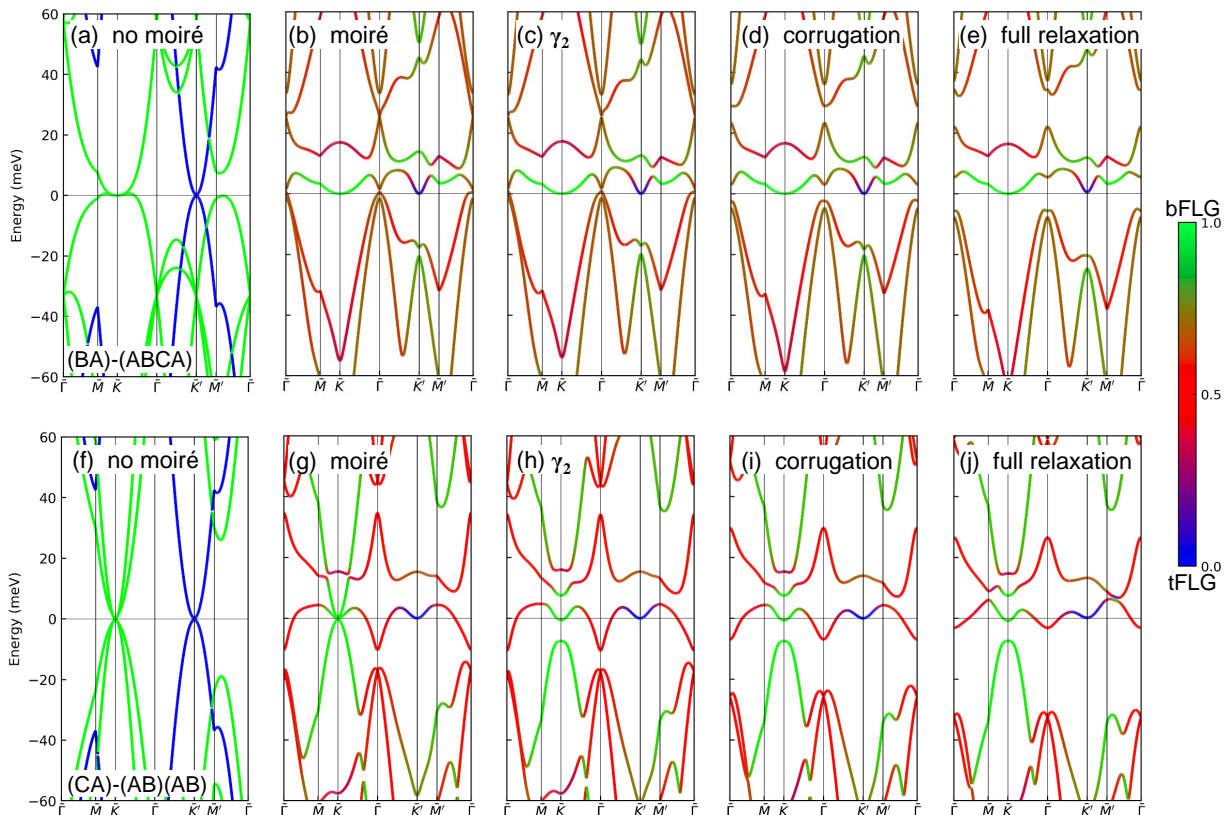


FIG. 3. (Color online) The band structures and state composition for TMLG with the (BA)-(ABCA) stacking (a-e) and the (CA)-(AB)(AB) stacking (f-j) at $\theta = 1.35^\circ$. Starting from the rigid superlattice without moiré coupling between the FLGs and without the γ_2 hopping in the FLGs (a, e), the moiré coupling (b, g), the γ_2 hopping terms (c, h), the corrugation effect (d, i), and the in-plane relaxation effect (e, j) are included in the Hamiltonian successively. The band energies are directly calculated by diagonalizing the Hamiltonian without energy shifting, so the Fermi levels do not necessarily lie at the zero energy here.

out-of-plane electric field may separate crossed bands locally for some configurations, while only a rather small Δ can enhance the gaps around the isolated flat bands slightly and a larger Δ tends to close these global gaps, as shown for example in Fig. S5 for the (BA)-(ABCA) and (BA)-(ABCA) configurations.

IV. VALLEY CHERN NUMBERS AND ORBITAL MAGNETIC MOMENTS

At an odd filling of an isolated flat band, spontaneous valley polarization may occur due to the electron-electron interaction³¹. If such a valley polarized band hosts a non-zero Chern number, the TMLG can support QAHC. The Chern numbers C of flat bands in the $\xi = +$ valley have been obtained explicitly by integral of the Berry curvature (Ω_z) in the supercell BZ as detailed in the SM, and the C of a band in the $\xi = -$ valley is just the opposite of that for $\xi = +$. Chern numbers are also calculated for separable flat bands which are separated from nearby bands by local gaps larger than 0.5 meV to characterize the dependence of C on stacking orders of

TMLG.

We also focus on the Chern numbers (C_v) of flat valence bands in the $\xi = +$ valley. Among all configurations with $M + N$ layers, the largest $|C_v|$ is $M + N - 1$. The largest $|C_v|$ can occur in certain configurations with isolated flat bands, such as those shown in Figs. 1(b) and 1(d) and listed in Table SI. We note that the isolated flat valence band in a configuration with 10 layers [see Fig. 1(d)] has $C_v = -9$, which is the largest magnitude of C_v for all considered TMLG with $N + M \leq 10$.

Systematic calculations of all configurations with different stackings and θ show that most flat valence bands with high C_v slightly overlap with other bands and such band overlapping is related to the layers numbers (M and N) of FLGs in TMLG, as illustrated in Fig. 5. The appearance of highest C_v generally becomes less likely with increasing $N+M$. For $N + M = 6$, more cases with $|C_v| = 5$ appear for $M = 4$ than for $M = 3$ as type-II stacking is only possible for $M = 4$. In contrast, there are much fewer cases with the largest $|C_v|$ for $M = 6$ than for $M = 5$ when $M + N = 10$, which is related to the occurrence of type-III configurations only for $M = 5$. We notice that it is mainly the overlapping of the va-

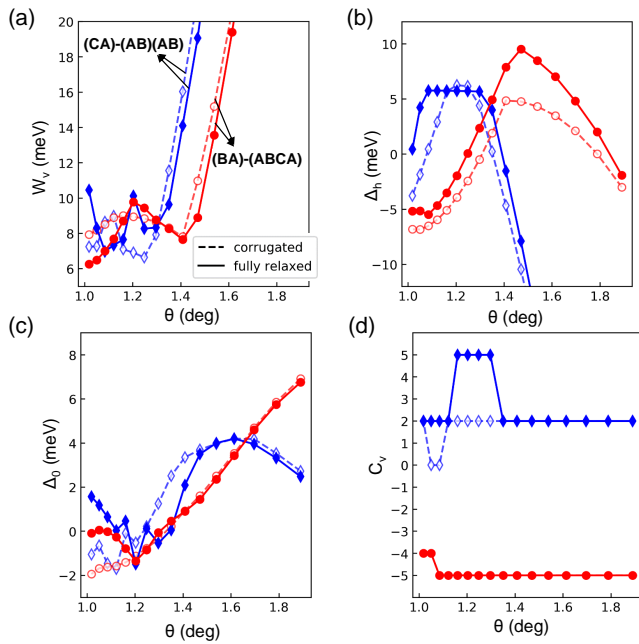


FIG. 4. (Color online) Variations of W_v (a), Δ_h (b), Δ_0 (c), and the Chern number (C_v) of the highest valence band (d) with θ for the (BA)-(ABCA) and (CA)-(AB)(AB) stackings considering full relaxation (solid symbols) or only corrugation (open symbols).

lence and conduction bands around EF, i.e. negative Δ_0 that keeps most flat valence bands from being isolated for large $N + M$.

By examining the evolution of Ω_z maps for the middle bands with the strength of the moiré coupling, we find that the large $|C_v|$ originates from the splitting of degenerate states by the weak moiré coupling or from the topological transitions induced by the strong coupling. With the decreasing θ the coupling between FLGs can be tuned from the weak to the strong regime. At a fixed θ , the coupling strength can be further reduced by rigidly increasing the average spacing (h_0) between FLGs.

Figure 6 displays the Ω_z maps of the valence and conduction bands around E_F for the (BA)-(ABCA) and (BA)-(ABCA) stacked configurations with different θ and h_0 . For (BA)-(ABCA) with $M = 4$ and $N = 2$, Ω_z peaks appear around \bar{K} and \bar{K}' in the weak coupling regime. The highest valence band states around \bar{K} (\bar{K}') are mainly contributed by the chiral bFLG (tFLG), whose Ω_z is integrated to be about $-M\pi$ ($-N\pi$)^{47,48}. Such integral values of Ω_z correspond to the Berry phases of the band states in a circle around a corner of the hexagonal BZ for the pristine FLGs, and the sign of the Berry phases is fixed by the fact that the valence state at \bar{K} (\bar{K}') is composed of non-dimer states in the bottom layer of bFLG (the top layer of tFLG) as discussed above. These Berry phases around \bar{K} and \bar{K}' contribute $-(M + N)/2 = -3$ to the total C_v for (BA)-(ABCA), and the Chern number (C_c) of the lowest conduction band gains a contribution

of 3. Moreover, the degeneracy lifting at the band crossings between the middle bands and the other bands gives rise to negative Ω_z peaks along three curves beginning from the Γ point for both the valence and conduction bands, and both C_v and C_c gain a contribution of -2 from these Ω_z peaks. Then C_v and C_c amount to -5 and 1, respectively. Similar to the 2D band dispersions, the distributions of Ω_z around \bar{K} and \bar{K}' exhibit trigonal warping inherited from the pristine chiral FLGs. With the decreasing θ or h_0 , the feathers of the Ω_z maps undergo great changes with the peaks merging, while the local gaps between the middle bands remain opened and the Chern numbers are maintained in a large range of θ , as seen in Fig. 4(d). Such evolution of Ω_z maps suggests that exploration of the electronic structure of TMLG in the weak regime of the moiré coupling is essential to interpret the origin of the Chern numbers at small θ . For some configurations with non-chiral FLGs, the largest $|C_v|$ can also be already present at large θ , such as the (BA)-(ABCA)(CB) stacking with $C_v = -7$ [see Fig. S6(a)] for θ from 1.89° to 1.47° at which the flat valence band becomes isolated.

In the weak coupling regime for (CA)-(AB)(AB), the Ω_z peaks around \bar{K}' originating from tFLG contribute +1 to C_v , while there are both positive and negative peaks around \bar{K} as bFLG is non-chiral, then C_v has a relatively small value of 2. With decreasing of θ , dipole-like pairs of positive and negative peaks form and band inversion between the middle bands occur at about 1.30° ,

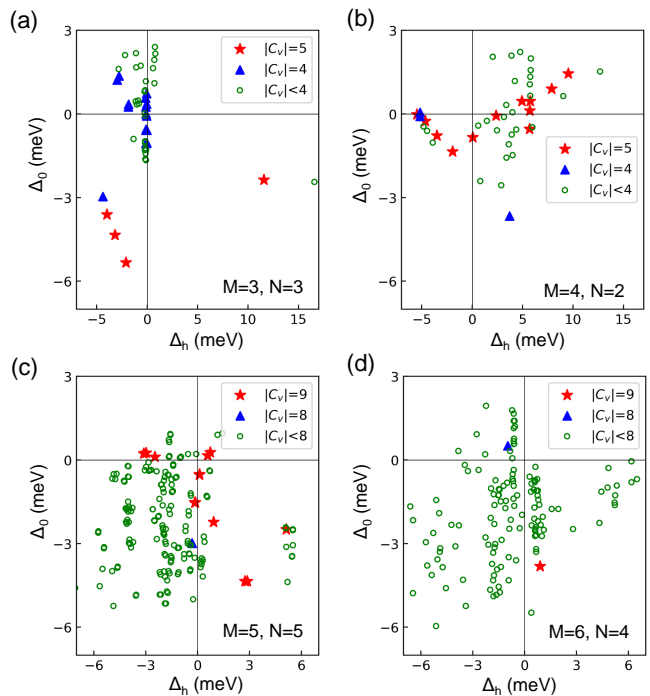


FIG. 5. (Color online) The $|C_v|$, Δ_0 and Δ_h of configurations with separable flat valence bands at given M and N . $M+N = 6$ in (a-b) and $M+N = 10$ in (c-d).

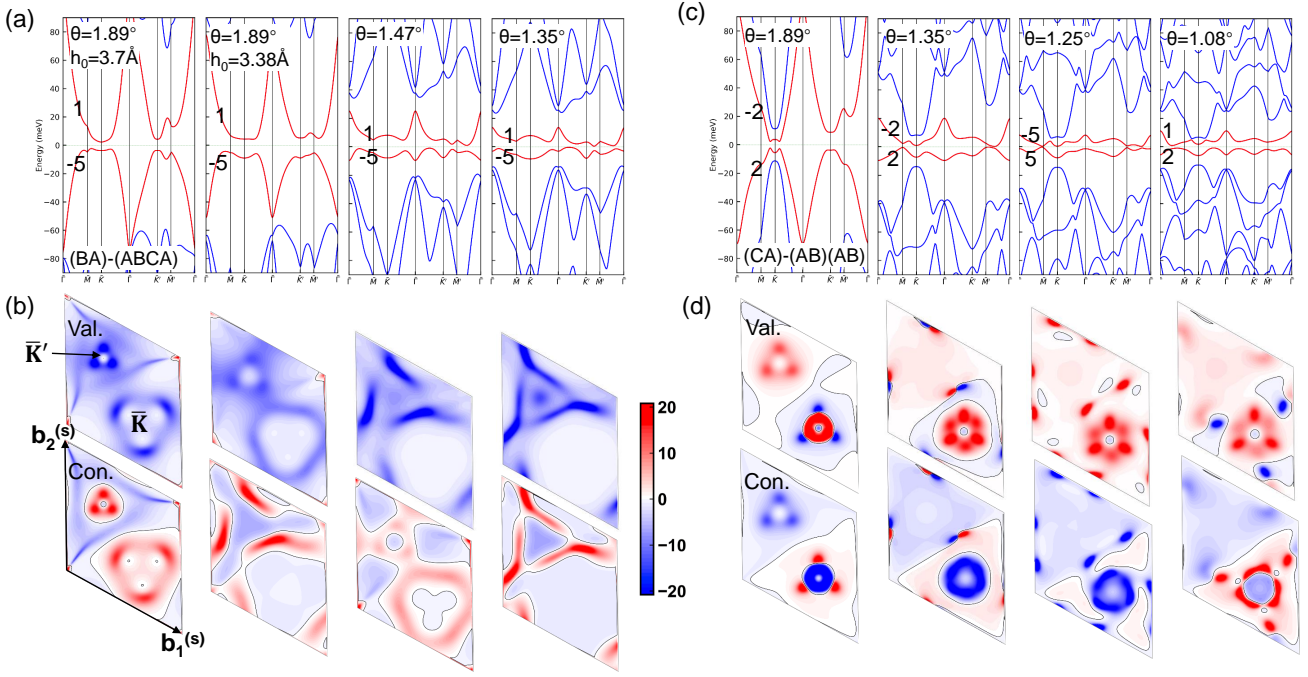


FIG. 6. (Color online) The band structures and Ω_z maps of the middle valence and conduction bands around E_F for the (BA)-(ABCA) (a-b) and the (BA)-(ABCA) (c-d) stackings with different θ and h_0 . In (a, c), the middle bands are displayed in red and their Chern numbers are labeled, and the Fermi levels are represented by dashed lines. In (b, d), the Ω_z maps are illustrated in the supercell BZ and the zero level of Ω_z is represented by gray contour lines.

leading to the largest C_v of 5. The next topological phase transition occurs at about 1.16° . We note that full relaxation is required to drive the topological phase transition with C_v rising to 5 in the strong coupling regime, as shown in Fig. 4(d). The $C_v = -9$ for the (CBA)(BA)-(AB)(ABC) stacking shown in Fig. 1(e) also occurs at small θ , and the variation of Ω_z maps with θ can be seen in Fig. S6(b).

The non-trivial topology in isolated flat bands suggests that spontaneous orbital magnetic moments (m) may be observed at odd fillings of the flat bands^{51,52}. We evaluate the magnitude of m contributed by the isolated flat valence band by setting the chemical potential at the middle of the Δ_0 gap. The magnitude of m can reach $10\mu_B$ per supercell for θ around 1.1° , as shown in Fig. 7(a). For configurations with positive m , its value is related to the layer numbers of TMLG with the $N+M=8$ cases generally having the largest m at a θ . m is roughly proportional to C_v , while the spanning of its value is still rather large for a given C_v , especially for small $|C_v|$. We note that for certain cases with a small $|m|$ but a large $|C_v|$, the sign of the total orbital magnetic moment may be inverted by tuning the chemical potential across the gap⁵¹.

V. SUMMARY AND CONCLUSIONS

For TMLG with $M+N$ layers, full relaxation has been performed for the 2^{M+N-3} inequivalent stacking orders at varying θ . Isolated flat bands emerge in relaxed TMLG with $M+N$ up to 10 and with various stackings, and most of them are on the hole side. The stacking orders that most isolated flat bands can be categorized into four types based on the electronic behavior of flat bands and the stacking decomposition. For type-I configurations with both chiral FLGs, the touched bands of FLGs around E_F are split by the moiré coupling through the electron-hole asymmetry in low-energy bands of FLGs while the hopping γ_2 between the next-nearest layers is further required for the state splitting in other types with non-chiral FLGs. The corrugation effect reduces the band overlapping around E_F and the full structural relaxation leads to global gaps that completely isolate a flat band. For TMLG with given M and N , the highest Chern number $|C|$ of the separable flat bands reaches $M+N-1$ and can be hosted by certain isolated bands. The $|C|=9$ occurs in the isolated flat valence band of several configurations with 10 layers. Such high $|C|$ originates from the lifting of the band-state degeneracy in the weak regime of moiré coupling or from the topological phase transitions induced by the strong moiré coupling. Moreover, large orbital magnetic moments m arise in isolated flat bands with high $|C|$ and depend on the structural configurations

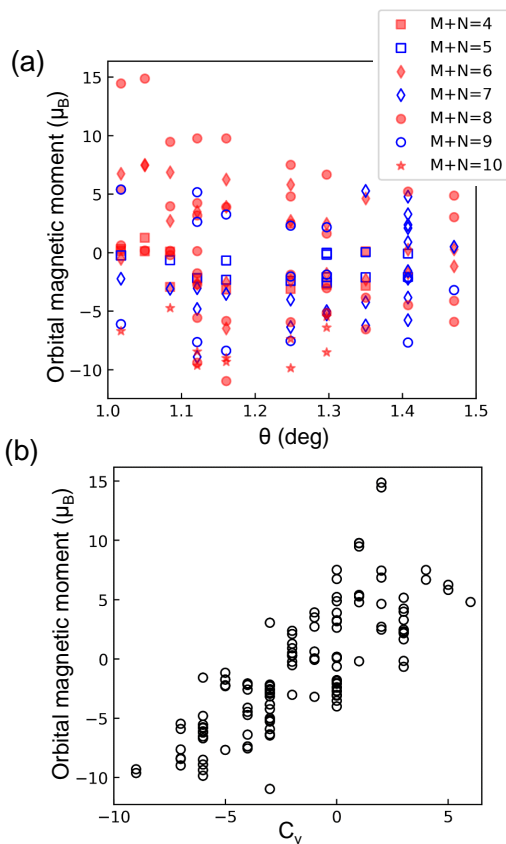


FIG. 7. (Color online) (a) The orbital magnetic moments (m) contributed by the isolated flat valence band for configurations with different layer numbers ($M + N$). (b) m versus C_v for all configurations with isolated flat valence bands.

of TMLG.

ACKNOWLEDGMENTS

We gratefully acknowledge valuable discussions with D. Tománek, H. Xiong, and S. Yin. This research was supported by the National Natural Science Foundation of China (Grants No. 11974312 and No. 11774195). The calculations were performed on TianHe-1(A) at National Supercomputer Center in Tianjin.

* E-mail: xqlin@zjut.edu.cn

¹ R. Bistritzer and A. H. MacDonald, “Moiré bands in twisted double-layer graphene,” *Proc. Natl. Acad. Sci. U.S.A.* **108**, 12233 (2011).

² J. M. B. Lopes dos Santos, N. M. R. Peres, and A. H. Castro Neto, “Continuum model of the twisted graphene bilayer,” *Phys. Rev. B* **86**, 155449 (2012).

³ S. Fang and E. Kaxiras, “Electronic structure theory of weakly interacting bilayers,” *Phys. Rev. B* **93**, 235153 (2016).

⁴ G. Tarnopolsky, A. Jura Kruchkov, and A. Vishwanath, “Origin of Magic Angles in Twisted Bilayer Graphene,” *Phys. Rev. Lett.* **122**, 106405 (2019).

⁵ Y. Cao, V. Fatemi, A. Demir, S. Fang, S. L. Tomarken, J. Y. Luo, J. D. Sanchez-Yamagishi, K. Watanabe, T. Taniguchi, E. Kaxiras, R. C. Ashoori, and P. Jarillo-Herrero, “Correlated insulator behaviour at half-filling in magic-angle graphene superlattices,” *Nature* **556**, 80 (2018).

⁶ Y. Cao, V. Fatemi, S. Fang, K. Watanabe, T. Taniguchi, E. Kaxiras, and P. Jarillo-Herrero, “Unconventional superconductivity in magic-angle graphene superlattices,” *Nature* **556**, 43 (2018).

⁷ X. Lu, P. Stepanov, W. Yang, M. Xie, M. A. Aamir, I. Das, C. Urgell, K. Watanabe, T. Taniguchi, G. Zhang, A. Bachtold, A. H. MacDonald, and D. K. Efetov, “Superconductors, orbital magnets, and correlated states in magic angle bilayer graphene,” *Nature* **574**, 653 (2019).

⁸ Y. Xie, B. Lian, B. Jäck, X. Liu, C.-L. Chiu, K. Watanabe, T. Taniguchi, B. A. Bernevig, and A. Yazdani, “Spectroscopic signatures of many-body correlations in magic-angle twisted bilayer graphene,” *Nature* **572**, 101 (2019).

⁹ A. Kerelsky, L. J. McGilly, D. M. Kennes, L. Xian, M. Yankowitz, S. Chen, K. Watanabe, T. Taniguchi, J. Hone, C. Dean, A. Rubio, and A. N. Pasupathy, “Maximized electron interactions at the magic angle in twisted bilayer graphene,” *Nature* **572**, 95 (2019).

¹⁰ Y. Jiang, X. Lai, K. Watanabe, T. Taniguchi, K. Haule, J. Mao, and E. Y. Andrei, “Charge order and broken rotational symmetry in magic-angle twisted bilayer graphene,” *Nature* **573**, 91 (2019).

¹¹ A. Uri, S. Grover, Y. Cao, J.A. Crosse, K. Bagani, D. Rodan-Legrain, Y. Myasoedov, K. Watanabe, T. Taniguchi, P. Moon, M. Koshino, P. Jarillo-Herrero, and E. Zeldov, “Mapping the twist-angle disorder and Landau levels in magic-angle graphene,” *Nature* **581**, 47

- (2020).
- 12 K. P. Nuckolls, M. Oh, D. Wong, B. Lian, K. Watanabe, T. Taniguchi, B. A. Bernevig, and A. Yazdani, “Strongly correlated Chern insulators in magic-angle twisted bilayer graphene,” *Nature* **588**, 610 (2020).
 - 13 E. Y. Andrei and A. H. MacDonald, “Graphene bilayers with a twist,” *Nat. Mater.* **19**, 1265 (2020).
 - 14 E. Y. Andrei, D. K. Efetov, P. Jarillo-Herrero, A. H. MacDonald, K. F. Mak, T. Senthil, E. Tutuc, A. Yazdani, and A. F. Young, “The marvels of moiré materials,” *Nat. Rev. Mater.* **6**, 201 (2021).
 - 15 Z. Song, Z. Wang, W. Shi, G. Li, C. Fang, and B. A. Bernevig, “All magic angles in twisted bilayer graphene are topological,” *Phys. Rev. Lett.* **123**, 036401 (2019).
 - 16 H. C. Po, L. Zou, T. Senthil, and A. Vishwanath, “Faithful tight-binding models and fragile topology of magic-angle bilayer graphene,” *Phys. Rev. B* **99**, 195455 (2019).
 - 17 J. Ahn, S. Park, and B.-J. Yang, “Failure of nielsen-nomiya theorem and fragile topology in two-dimensional systems with space-time inversion symmetry: Application to twisted bilayer graphene at magic angle,” *Phys. Rev. X* **9**, 021013 (2019).
 - 18 J. Liu, J. Liu, and X. Dai, “Pseudo landau level representation of twisted bilayer graphene: Band topology and implications on the correlated insulating phase,” *Phys. Rev. B* **99**, 155415 (2019).
 - 19 N. Bultinck, S. Chatterjee, and M. P. Zaletel, “Mechanism for Anomalous Hall Ferromagnetism in Twisted Bilayer Graphene,” *Phys. Rev. Lett.* **124**, 166601 (2020).
 - 20 Y.-H. Zhang, D. Mao, and T. Senthil, “Twisted bilayer graphene aligned with hexagonal boron nitride: Anomalous Hall effect and a lattice model,” *Phys. Rev. Research* **1**, 033126 (2019).
 - 21 J. Liu and X. Dai, “Anomalous Hall effect, magneto-optical properties, and nonlinear optical properties of twisted graphene systems,” *npj Comput. Mater.* **6**, 57 (2020).
 - 22 X. Lin and J. Ni, “Symmetry breaking in the double moiré superlattices of relaxed twisted bilayer graphene on hexagonal boron nitride,” *Phys. Rev. B* **102**, 035441 (2020).
 - 23 T. Cea, P. A. Pantaleón, and F. Guinea, “Band structure of twisted bilayer graphene on hexagonal boron nitride,” *Phys. Rev. B* **102**, 155136 (2020).
 - 24 X. Lin, K. Su, and J. Ni, “Misalignment instability in magic-angle twisted bilayer graphene on hexagonal boron nitride,” *2D Mater.* **8**, 025025 (2021).
 - 25 J. Shi, J. Zhu, and A. H. MacDonald, “Moiré commensurability and the quantum anomalous Hall effect in twisted bilayer graphene on hexagonal boron nitride,” *Phys. Rev. B* **103**, 075122 (2021).
 - 26 D. Mao and T. Senthil, “Quasiperiodicity, band topology, and moiré graphene,” *Phys. Rev. B* **103**, 115110 (2021).
 - 27 M. Serlin, C. L. Tschirhart, H. Polshyn, Y. Zhang, J. Zhu, K. Watanabe, T. Taniguchi, L. Balents, and A. F. Young, “Intrinsic quantized anomalous Hall effect in a moiré heterostructure,” *Science* **367**, 900 (2020).
 - 28 A. L. Sharpe, E. J. Fox, A. W. Barnard, J. Finney, K. Watanabe, T. Taniguchi, M. A. Kastner, and D. Goldhaber-Gordon, “Emergent ferromagnetism near three-quarters filling in twisted bilayer graphene,” *Science* **365**, 605 (2019).
 - 29 G. Chen, A. L. Sharpe, E. J. Fox, Y.-H. Zhang, S. Wang, L. Jiang, B. Lyu, H. Li, K. Watanabe, T. Taniguchi, Z. Shi, T. Senthil, D. Goldhaber-Gordon, Y. Zhang, and F. Wang, “Tunable correlated Chern insulator and ferromagnetism in a moiré superlattice,” *Nature* **579**, 56 (2020).
 - 30 J. Y. Lee, E. Khalaf, S. Liu, X. Liu, Z. Hao, P. Kim, and A. Vishwanath, “Theory of correlated insulating behaviour and spin-triplet superconductivity in twisted double bilayer graphene,” *Nat. Commun.* **10**, 5333 (2019).
 - 31 Y.-H. Zhang, D. Mao, Y. Cao, P. Jarillo-Herrero, and T. Senthil, “Nearly flat Chern bands in moiré superlattices,” *Phys. Rev. B* **99**, 075127 (2019).
 - 32 J. Liu, Z. Ma, J. Gao, and X. Dai, “Quantum Valley Hall Effect, Orbital Magnetism, and Anomalous Hall Effect in Twisted Multilayer Graphene Systems,” *Phys. Rev. X* **9**, 031021 (2019).
 - 33 M. Koshino, “Band structure and topological properties of twisted double bilayer graphene,” *Phys. Rev. B* **99**, 235406 (2019).
 - 34 N. R. Chebrolu, B. L. Chittari, and J. Jung, “Flat bands in twisted double bilayer graphene,” *Phys. Rev. B* **99**, 235417 (2019).
 - 35 X. Lin, H. Zhu, and J. Ni, “Pressure-induced gap modulation and topological transitions in twisted bilayer and twisted double bilayer graphene,” *Phys. Rev. B* **101**, 155405 (2020).
 - 36 A. Vela, M. V. O. Moutinho, F. J. Culchac, P. Venezuela, and R. B. Capaz, “Electronic structure and optical properties of twisted multilayer graphene,” *Phys. Rev. B* **98**, 155135 (2018).
 - 37 T. Cea, N. R. Walet, and F. Guinea, “Twists and the electronic structure of graphitic materials,” *Nano Lett.* **19**, 8683–8689 (2019).
 - 38 G. A. Tritsarlis, S. Carr, Z. Zhu, Y. Xie, S. B. Torrisi, J. Tang, M. Mattheakis, D. T. Larson, and E. Kaxiras, “Electronic structure calculations of twisted multi-layer graphene superlattices,” *2D Mater.* **7**, 035028 (2020).
 - 39 S. Zhang, B. Xie, Q. Wu, J. Liu, and O. V. Yazyev, “Chiral decomposition of twisted graphene multilayers with arbitrary stacking,” [arXiv:2012.11964](https://arxiv.org/abs/2012.11964).
 - 40 J. Cao, M. Wang, C.-C. Liu, and Y. Yao, “*Ab initio* four-band Wannier tight-binding model for generic twisted graphene systems,” [arXiv:2012.02575](https://arxiv.org/abs/2012.02575).
 - 41 Z. Ma, S. Li, M.-M. Xiao, Y.-W. Zheng, M. Lu, H. Liu, J.-H. Gao, and X. C. Xie, “Moiré flat bands of twisted few-layer graphite,” [arXiv:2001.07995](https://arxiv.org/abs/2001.07995).
 - 42 N. N. T. Nam and M. Koshino, “Lattice relaxation and energy band modulation in twisted bilayer graphene,” *Phys. Rev. B* **96**, 075311 (2017).
 - 43 H. Yoo, R. Engelke, S. Carr, S. Fang, K. Zhang, P. Cazeaux, S. H. Sung, R. Hovden, A. W. Tsen, T. Taniguchi, K. Watanabe, G.-C. Yi, M. Kim, M. Luskin, E. B. Tadmor, E. Kaxiras, and P. Kim, “Atomic and electronic reconstruction at the van der Waals interface in twisted bilayer graphene,” *Nat. Mater.* **18**, 448 (2019).
 - 44 P. Lucignano, D. Alfè, V. Cataudella, D. Ninno, and G. Cantele, “Crucial role of atomic corrugation on the flat bands and energy gaps of twisted bilayer graphene at the magic angle $\theta \sim 1.08^\circ$,” *Phys. Rev. B* **99**, 195419 (2019).
 - 45 F. Guinea and N. R. Walet, “Continuum models for twisted bilayer graphene: Effect of lattice deformation and hopping parameters,” *Phys. Rev. B* **99**, 205134 (2019).
 - 46 Y. W. Choi and H. J. Choi, “Intrinsic band gap and electrically tunable flat bands in twisted double bilayer graphene,” *Phys. Rev. B* **100**, 201402 (2019).
 - 47 M. Koshino and E. McCann, “Trigonal warping and berry’s phase $N\pi$ in abc-stacked multilayer graphene,” *Phys. Rev. B* **80**, 165409 (2009).

- ⁴⁸ F. Zhang, B. Sahu, H. Min, and A. H. MacDonald, “Band structure of *abc*-stacked graphene trilayers,” *Phys. Rev. B* **82**, 035409 (2010).
- ⁴⁹ H. Min and A. H. MacDonald, “Chiral decomposition in the electronic structure of graphene multilayers,” *Phys. Rev. B* **77**, 155416 (2008).
- ⁵⁰ H. Min and A. H. MacDonald, “Electronic structure of multilayer graphene,” *Progress of Theoretical Physics Supplement* **176**, 227 (2008).
- ⁵¹ J. Zhu, J.-J. Su, and A. H. MacDonald, “Voltage-Controlled Magnetic Reversal in Orbital Chern Insulators,” *Phys. Rev. Lett.* **125**, 227702 (2020).
- ⁵² C. Repellin, Z. Dong, Y.-H. Zhang, and T. Senthil, “Ferromagnetism in narrow bands of moiré superlattices,” *Phys. Rev. Lett.* **124**, 187601 (2020).